OPEN

Correspondence and requests for materials should be addressed to Y.-H.W. (yhwen@xmu. edu.cn)

Diverse Melting Modes and Structural Collapse of Hollow Bimetallic Core-Shell Nanoparticles: A Perspective from Molecular Dynamics Simulations

Rao Huang[1], Gui-Fang Shao[2], Xiang-Ming Zeng[1] & Yu-Hua Wen[1]

[1]Institute of Theoretical Physics and Astrophysics, Department of Physics, Xiamen University, Xiamen, 361005, China, [2]Center for Cloud Computing and Big Data, Department of Automation, Xiamen University, Xiamen, 361005, China.

Introducing hollow structures into metallic nanoparticles has become a promising route to improve their catalytic performances. A fundamental understanding of thermal stability of these novel nanostructures is of significance for their syntheses and applications. In this article, molecular dynamics simulations have been employed to offer insights into the thermodynamic evolution of hollow bimetallic core-shell nanoparticles. Our investigation reveals that for hollow Pt-core/Au-shell nanoparticle, premelting originates at the exterior surface, and a typical two-stage melting behavior is exhibited, similar to the solid ones. However, since the interior surface provides facilitation for the premelting initiating at the core, the two-stage melting is also observed in hollow Au-core/Pt-shell nanoparticle, remarkably different from the solid one. Furthermore, the collapse of hollow structure is accompanied with the overall melting of the hollow Pt-core/Au-shell nanoparticle while it occurs prior to that of the hollow Au-core/Pt-shell nanoparticle and leads to the formation of a liquid-core/solid-shell structure, although both of them finally transform into a mixing alloy with Au-dominated surface. Additionally, the existence of stacking faults in the hollow Pt-core/Au-shell nanoparticle distinctly lowers its melting point. This study could be of great importance to the design and development of novel nanocatalysts with both high activity and excellent stability.

N oble metallic nanocatalysts represent an important class of architectures in catalysis owing to their superior catalytic properties[1–2]. However, the rare reserve and extremely high price greatly limit their further wide use. Aiming to meet the growing demand in industry, a key issue is to develop new types of noble metallic based nanocatalysts with enhanced activity and improved utilization efficiency. To achieve this goal, an important strategy is to introduce other metal(s) into noble metallic nanocatalysts selectively. Recent advances have revealed that bimetallic and multimetallic nanoparticles (NPs) are able to possess better catalytic properties than the corresponding monometallic ones[3–12]. For example, Au-Pt core-shell bimetallic NPs exhibited higher electrocatalytic activity and durability for oxygen reduction reactions (ORR) than Pt monometallic catalysts[6]. Moreover, the superior activities of both Pt-Ru and Pt-Rh bimetallic NPs were also ascertained in preferential oxidation of CO in hydrogen (PROX)[9]. On the other hand, as another route for reducing the precious metal loadings, introducing hollow structures into the particles has recently received increasing attention[13–16]. This procedure provides enormous opportunities for developing novel and exceptional properties[17,18]. When the NP is hollow, the catalytic reactions may take place at both the surface and the cavity, leading to enhancing catalytic activity and lowering cost of raw material. Available studies have verified that hollow Pt NPs exhibit a larger surface area and enhanced electrocatalytic performance for methanol oxidation reaction (MOR) in comparison with solid Pt ones[14]. Moreover, hollow Ru NPs exhibited enhanced catalytic activity in the dehydrogenation of ammonia borane compared with solid ones[15]. Currently, bimetallic NPs with interior hollows have also been successively synthesized to further improve their utilization efficiency[19–25]. These novel NPs present even more superior catalytic performance, which should be highly promising for industry applications. For instance, hollow Au-Pt core-shell NPs display better catalytic activities as electrocatalysts than hollow Pt NPs, and hollow Au-Pd core-shell NPs show the highest current density for the ethanol oxidation reactions (EOR) in alkaline medium[19]. The Pt-Pd nanocages with a hollow interior and porous dendritic shell show superior catalytic activity

1

for MOR compared to other Pt-based catalysts reported previously[20]. The significant enhancement in catalytic activity has been attributed to the synergy effect of increased surface area and electronic structure of the alloy.

With hybrid metallic NPs becoming a new catalytic species, hollow core-shell NPs are expected to be more fascinating materials than solid ones due to their structural characteristics. Nevertheless, a large number of catalytic reactions take places in high-temperature conditions, especially in the cracking of petroleum and the purification of automobile exhaust gases. Considering the potential application of hollow bimetallic NPs as an important class of nanocatalysts, a thorough investigation on their thermodynamic stability thus becomes a crucial issue. As is known, the introduction of interior hollows will bring a profound influence on the microstructure of the particles. For example, twin boundaries were hardly observed in the experimentally prepared hollow Au NPs, although they frequently occurred in solid noble metallic NPs[19]. This is generally attributed to the hollow interior remarkably reducing the strain energy of Au lattice planes. Naturally, it is expectable that hollow bimetallic NPs will exhibit prominent differences in microstructure and thermodynamic behaviors compared with the solid ones. Furthermore, some significant phenomena such as shrinkage or collapse of hollow nanostructure may also become possible at elevated temperatures, which will strongly affect their chemical and physical properties. However, although there are available studies on synthesis, characterization and catalytic performance of hollow bimetallic NPs, less is known about their morphologies at various temperatures. The main reason for the absence of the relevant research lies in that it is quite difficult or even impossible to experimentally capture the atomistic structure evolution of these NPs under continuous heating. Fortunately, the rapid development of the current calculation capacity make computer simulations become popular in exploring the physical and chemical properties of metal NPs, remedying the deficiency of experiments.

In this article, we performed molecular dynamics (MD) simulations to investigate the thermodynamic behavior and microstructural evolution of hollow bimetallic NPs under continuous heating. Two types of NPs were considered here, i.e., hollow Au-core/Pt-shell (denoted as Au@Pt) and the inverted hollow Pt-core/Au-shell (denoted as Pt@Au) NPs. More accurately speaking, the "core" is actually the inner shell around the cavity, as seen in Figure 1 for their detailed structures. Hollow Au and Pt NPs were also structured for comparison. It should be noted that the hollow structures are difficult to be clearly exposed from Figure 1 (b) and (c) because the cavities are fully surrounded by the cores and shells, unlike one-dimensional hollow nanowires or two-dimensional hollow disks.

These NPs were heated to high temperatures to examine their thermodynamic evolution and associated behaviors. The caloric curves were first calculated and the solid-liquid phase transition was identified. Subsequently, the melting process was analyzed, and diverse melting modes were discovered. Finally, the stacking faults and structural collapse were investigated according to the stress distribution and statistical radius during continuous heating. To the best of our knowledge, this is the first report about their thermal stability and morphology evolution at atomistic level.

Results and Discussion

In a continuous heating process, the solid-liquid phase transition can be well demonstrated by the caloric curves, as seen in Figure 2. Note that the heat capacity was deduced according to the following equation[26]

$$C_p(T) = \frac{dU}{dT} + \frac{3}{2}R_{gc}, \tag{1}$$

where U is potential energy, and $R_{gc} = 8.314$ J/(molK). For facilitating comparison, the results of hollow Au and Pt NPs are also illustrated in Figure 2.

It can be found from Figure 2 that the caloric curves of hollow monometallic particles are similar to those of solid ones which has been extensively investigated[26]: The phase transition occurs at the temperature where the potential energy shows a sharp rise and the heat capacity accordingly displays an abrupt peak (1080 K for Au NP and 1850 for Pt NP). In contrast, there exist two distinct peaks in both bimetallic NPs, which generally indicates the occurrence of "two-stage" melting[27]. The critical temperatures T_m for the two stages of melting are respectively 1140 K and 1660 K for Au@Pt NP, and are 1030 K and 1430 K for Pt@Au NP. The two-stage melting should be originated from the relatively large difference of T_m between Au and Pt (1337 K and 2045 K for their bulks[28]). However, the two-stage melting was not observed in solid Au-core/Pt-shell NPs with different core/shell ratios[29], suggesting that the large difference of T_m between the components in bimetallic NP does not necessarily lead to the occurrence of two-stage melting. The geometry of the particle, especially the hollow structure, plays a dominant role in determining its melting mode (see the detailed discussion later). Additionally, it also should be noted that, remarkably different from the monometallic NPs, the potential energies of hollow core-shell NPs decreased to various extents at around the melting temperatures, manifesting the negative heat capacity. Furthermore, there are significant differences between the two bimetallic NPs: The negative heat capacity occurs at both stages of melting in the hollow Au@Pt NP, while only exists at the second stage in the hollow Pt@Au one. Another interesting phenomenon is that the melting temperatures of the hollow Au@Pt NP lie between that of hollow Au NP (1080 K) and that of hollow Pt NP (1850 K), however, the critical temperature of the first stage melting of the hollow Pt@Au NP (1030 K) is even lower than that of the hollow Au one. This implies that the existence of Pt core does not enhance the thermal stability of pure Au shell. The reason for these interesting discrepancies should be closely associated with the different melting processes of these two NPs.

In order to thoroughly explore the thermal-driven behaviors of these hollow NPs and to gain an in-depth understanding of their melting mechanisms, a simple but effective measurement, the Lindemann index, was introduced to characterize the thermal evolution in the heating process. It can provide a good description for the thermally driven disorder of a system. For the system of N atoms, the local Lindemann index for the ith atom is defined as the root-mean-squared (RMS) bond length fluctuation as[30]

$$\delta_i = \frac{1}{N-1} \sum_{j \neq i} \frac{\sqrt{\langle R_{ij}^2 \rangle - \langle R_{ij} \rangle^2}}{\langle R_{ij} \rangle}, \tag{2}$$

and the system-averaged Lindemann index is calculated by

$$\delta = \frac{1}{N} \sum_i \delta_i, \tag{3}$$

where R_{ij} is the distance between the ith and jth atoms. The Lindemann index was originally developed to study the melting behavior of bulk crystals. The Lindemann criterion suggests that the melting occurs when the index is in the range of 0.1–0.15, depending on materials[31], while a smaller criterion index of about 0.03–0.05 was adopted in nanoclusters and homopolymers due to the relaxed constraint of surface atoms[32]. By analyzing the temperature-dependent Lindemann indices of the hollow Au and Pt NPs during the heating process (not presented here), it can be found that the critical indices of 0.0335 and 0.0344 are respectively appropriate for Au and Pt components. Note that the determination of critical value has been elaborated in our previous works[27,29]. Based on these two critical values, the concept of Lindemann atom was introduced: The atom whose Lindemann index exceeds its critical value was defined as Lindemann atom, otherwise, non-Lindemann atom. For visualizing the melting process at atomic level, the snapshots of the two
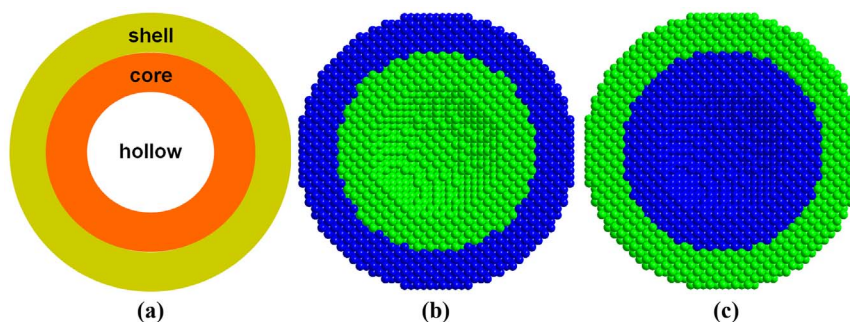
Figure 1 | (a) Schematic illustration of core-shell NPs with hollow structures and atomic arrangement of cross-section of (b) hollow Au@Pt NPs and (c) hollow Pt@Au NPs. Coloring denotes type of atom: green, Au atom; blue, Pt atom.

hollow bimetallic NPs at representative temperatures extracted from data records calculated by MD simulations and the corresponding distributions of Lindemann indices were illustrated in Figure 3.

Evidently, a typical two-stage melting in these two NPs can be verified from Figure 3a and 3b, respectively, consistent with the results of the potential energy and capacity heat in Figure 2. For the hollow Au@Pt NP, one can observe that the interior Au core started the melting earlier (at around 1130 K) than the Pt shell, corresponding to the first stage melting. However, it has been revealed by our previous study that in the solid Au@Pt NPs, the melting always originates from the Pt surface and then gradually spreads into the Au core[29], although the bulk melting temperature of Au is significantly lower than that of Pt (1337 K for the former and 2045 K for the latter)[28]. The reason for this discrepancy should be chiefly attributed to the existence of hollow structure. Similar to those atoms at the exterior surface, the ones located at the interior surface are also low-coordinated and have weaker bonding. Therefore, the presence of hollow structure makes it possible for the premelting to start from the interior surface, thus further initiating the melting of the core (see the second and third snapshots in Figure 3a). This is also why the premetling occurs in both the interior and exterior surfaces almost simultaneously in hollow Au and Pt NPs. (The corresponding snapshots are not presented here.) Moreover, it should be noted from the distribution of Lindemann indices of the hollow Au@Pt NP at 1130 K that many Au atoms has diffused across the initial boundary of the cavity and come into the hollow region. This trend is further expanded with the rising temperatures. As we know, the potential energies of the surface atoms are higher than that of the interior ones. Consequently, the total potential energy of particle will decrease

Figure 2 | Temperature dependence of potential energy (solid lines) and the corresponding heat capacities (dashed lines) of hollow monometallic and bimetallic NPs.

rapidly with the interior surface shrinking, leading to the negative heat capacity (see Figure 2).

By comparison, for the hollow Pt@Au NP, the reduction of the surface area of the cavity did not happen until the second stage melting (see the third and fourth snapshots in Figure 3b), which is the reason for the negative heat capacity only appearing at the second stage of melting. Besides, the decreasing potential energy in the second stage of melting for the Au@Pt NP should be originated from the discrepancy of surface energy between the two components. It is known that the particles have the tendency to form a low-energy structure[33]. Therefore, Au atoms tend to aggregate at the surfaces and Pt ones are preferentially distributed in the interior, since Au has much lower surface energy than Pt (the experimental value is 1.506 J/m^{2} for the former and 2.489 J/m^{2} for the latter)[34], as shown in the fifth snapshots in Figure 3a and 3b. This inhomogeneous distribution has also been ascertained in our previous investigations on other bimetallic systems[35,36].

As is aforementioned, the melting temperature of the first stage of the hollow Pt@Au NP is even lower than that of pure hollow Au NP. This suggests that the alloying of Pt does not enhance the thermal stability of Au shell, which seems to contradict the commonsense intuition because the melting point of Pt is significantly higher than that of Au. To disclose the reason for this phenomenon, we explored the structural evolution of these NPs during continuous heating. Here, the common neighbor analysis (CNA), proposed by Honeycutt and Andersen[37], was employed to characterize the local crystal structure in NPs. This method has already been extensively adopted to analyze the structural evolution of nanomaterials during the mechanical deformation and melting process[38,39]. To determine the crystal structure, the bonds between an atom and its nearest neighbors were examined. Utilizing this analysis, all the atoms in a NP were classified into three categories: Atoms in a local fcc order were considered to be fcc atoms; atoms in a local hcp order were classified as hcp atoms, whose occurrence in an fcc crystal is generally regarded as the structure of stacking faults; atoms in all other local orders were considered to be "other" atoms since they did not reveal any useful information in fcc NPs.

Figure 4a illustrates the temperature dependence of percentages of hcp atoms in the four hollow NPs. Apparently, the bimetallic NPs show completely different behaviors in comparison with the monometallic ones. For monometallic particles, hcp atoms existed only at around their melting points (1080 K for Au and 1850 K for Pt), and their percentages were rather small (less than 0.4%). Since these hcp atoms were discretely distributed in the whole particle and did not aggregate to form ordered structure, their presence did not signify the formation of stacking faults during the heating process. On the contrary, hcp atoms massively occurred in the bimetallic NPs within much broader temperature ranges and were regularly arranged in a series of two adjacent {111} planes to form the structure of intrinsic stacking faults (see the insets in Figure 4a). In terms of the theory of
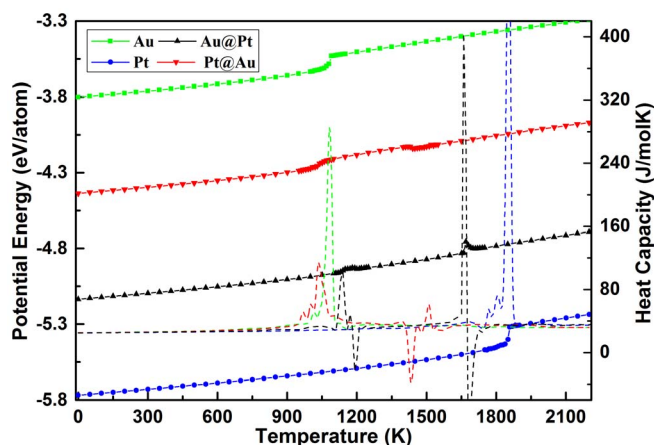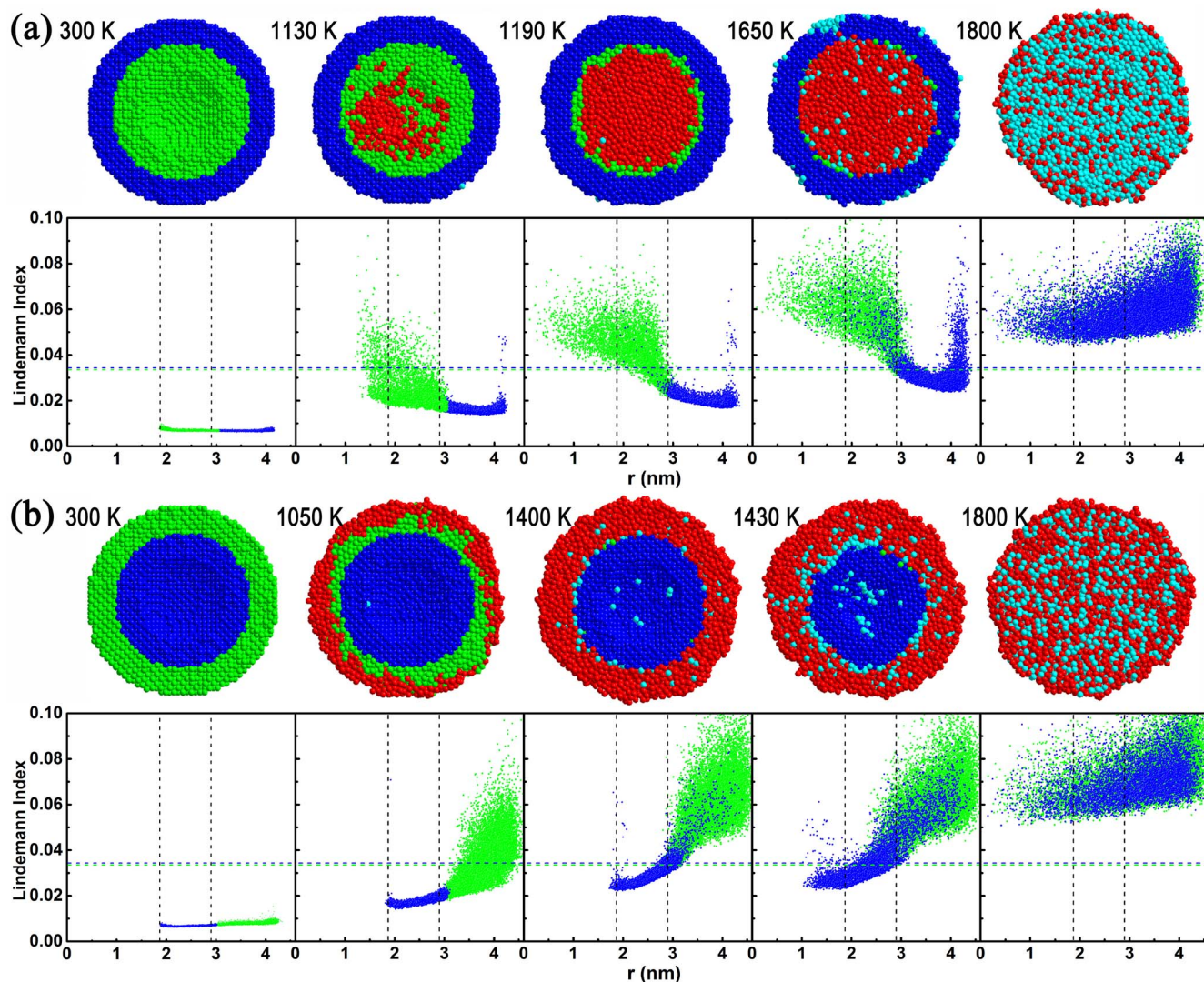
Figure 3 | Snapshots of cross sections of hollow (a) Au@Pt and (b) Pt@Au NPs taken at five representative temperatures. Coloring denotes type of atoms: green, Au non-Lindemann atom; blue, Pt non-Lindemann atom; red, Au Lindemann atom; cyan, Pt Lindemann atom. The Lindemann index distributions of atoms at corresponding temperatures are also exhibited below the snapshots. Note that the horizontal axis denotes the distance between the atom and the particle center of mass. The vertical dashed lines denote the initial boundary of the hollow structure and the interface between core and shell. The horizontal dashed lines indicate the critical Lindemann indices: 0.0335 for Au and 0.0344 for Pt.

crystal dislocations, the intrinsic stacking fault will be produced once a Shockley partial dislocation nucleates and propagates through an fcc crystal[40]. Resultantly, the accumulated stress could be partly released by the activity of the partial dislocations[29]. As seen in Figure 4a, there exist two peaks in each curve, which should be associated with the two-stage melting of the bimetallic particles. More importantly, the hollow Pt@Au NP greatly differs from the hollow Au@Pt one in terms of the atomic arrangement. The stacking faults did not emerge in the hollow Au@Pt NP until a relatively high temperature (650 K here), while they occurred in the hollow Pt@Au one at low temperatures, as indicated by Figure 4a. It can be seen that at 300K, two adjacent {111} planes of hcp atoms extending from the Pt-core/Au-shell interface toward the exterior surface of Au shell were clearly identified as intrinsic stacking faults. Owing to the fact that the presence of these intrinsic stacking faults broke the periodic fcc arrangement in Au shell, it is naturally observed that the T_m of the first stage melting of the hollow Pt@Au NP was even lower than the T_m of the hollow Au NP (1030 K for the former and 1080 K for the latter). With the rising temperature, the stress accumulated in the NPs was further released through the activities of Shockley

partial dislocations, resulting in the formation of more stacking faults and the production of more hcp atoms (see the snapshot at 900 K inserted in Figure 4a). For a solid bimetallic core-shell NP, the stacking faults are generally distributed in the shell and terminated at the interface and surface[29]. However, it can be noted here that hcp atoms also widely appeared in the Pt core and some of the stacking faults passed through the whole particle. This result is associated with the interior surface of the hollow NPs. Its existence facilitates the nucleation and propagation of partial dislocations.

To further clarify the origination of the stacking faults of hollow core-shell NP, we calculated the local stress in the two bimetallic NPs. The local stress σ_n at the ith atom site can be written as

$$\sigma_n = \frac{1}{3}\sum_{\alpha=1}^{3}\sigma_{\alpha\alpha} = \frac{1}{3}\sum_{\alpha=1}^{3}\left(\frac{1}{2\Omega_i}\sum_{j\neq i}F_{ij}^{\alpha}R_{ij}^{\alpha}\right), \qquad (4)$$

where F_{ij} and R_{ij} are the force and distance between atoms i and j. Ω_i is the local volume between atom i and all its neighbor atoms[41].

The stress distributions of the two NPs at 300 K are illustrated in Figure 4b and 4c. Evidently, the atoms near the exterior and interior
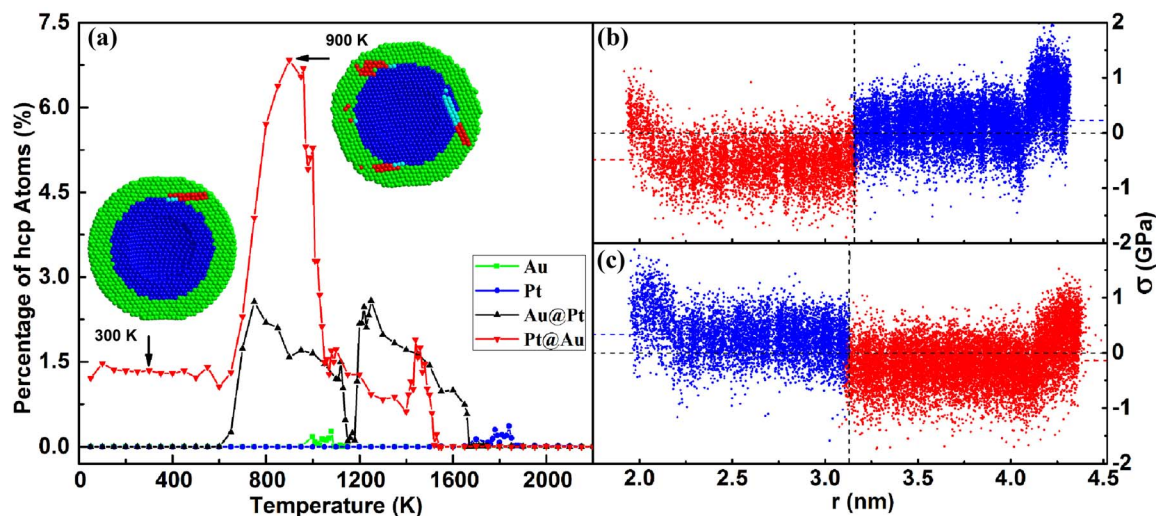
Figure 4 | (a) Temperature-dependent percentage of hcp atoms in the hollow monometallic and bimetallic NPs. (Insets) Snapshots of cross sections of the Pt@Au NP at 300 and 900 K. Coloring denotes atomic type: green, Au atom; blue Pt atom; red, hcp Au atom; cyan, hcp Pt atom. The stress distributions in core and shell at 300 K for (b) the hollow Au@Pt and (c) the hollow Pt@Au NPs are also illustrated on the right side. Note that the horizontal axis denotes the distance between the atom and the particle center of mass. The vertical dashed line denotes the core-shell interface while the horizontal dashed lines indicate the zero value, the average stresses in the core and in the shell, respectively.

surfaces basically possessed positive values, signifying the existence of surface tension. In the hollow Au@Pt NP, the majority of atoms were under compressive stress in the Au core while tensile stress in the Pt shell (The average stresses are -0.485 and 0.232 GPa, respectively, as denoted by the dashed lines.). However, the trend was opposite in the hollow Pt@Au NP: The average stresses were 0.330 GPa for the Pt core and -0.137 GPa for the Au shell. This difference should be mainly resulted from the difference in the linear thermal expansion coefficient between Au and Pt. As we know, the bulk value are 14.2×10^{-6} K^{-1} for Au and 8.8×10^{-6} K^{-1} for Pt, respectively[42]. During the heating process, the Au atoms will be subjected to strong confinement from the Pt ones by the core-shell interface since Au lattice expands faster than Pt lattice. Hence, Au atoms are always under compressive stress no matter in the core or in the shell. Besides, the lattice constant of Au is also larger than that of Pt (4.0782 Å for Au and 3.9242 Å for Pt), the lattice mismatch lead to the occurrence of stress step at the interface. Considering the different stress distributions in these two bimetallic NPs, it is not surprising that the nucleation and propagation of dislocations displayed diverse behaviors, leading to different temperature dependences of stacking faults (see Figure 4a).

Finally, in order to obtain an intuitive picture of atomic diffusion in these hollow NPs during the continuous heating, the concept of statistical radius was introduced into this work by the following equation[26]

$$R_N = \sqrt{\frac{5}{3}\frac{1}{N}\sum_{j=1}^{N}(R_j - R_{cm})^2}, \tag{5}$$

where (R_j-R_{cm}) is the distance of atom j from the particle center of mass. The temperature dependent statistical radii of both the hollow monometallic and bimetallic NPs are exhibited in Figure 5.

For the hollow Au and Pt NPs, the statistical radius linearly increased at low temperatures, which is usually attributed to the thermal expansion of lattice. The coefficients of linear thermal expansion, deduced from the statistical radius, are about 2.36×10^{-5} K^{-1} and 1.48×10^{-5} K^{-1} for Au and Pt NPs, respectively. Comparing with the corresponding bulk values, the thermal expansion coefficients of particles are significantly increased with their sizes decreasing to nanoscale, which has been confirmed by the

experiments on Au NPs[43]. With the temperature further rising, the statistical radius abruptly fell down at the melting points (1080 K for Au and 1850 K for Pt). This result was originated from the shrinkage and collapse of the hollow structure in the NPs. Hereafter, it resumed linear increasing with a bigger slope, indicating the larger expansion coefficient of liquid NP than that of solid one. Moreover, it can be noted from the curves that before the melting points, the statistical radii were gradually deviated from the initial linear increase. This was also caused by the faster thermal expansion of the melted liquid than that of the remaining solid.

By comparison, the situations in the hollow bimetallic NPs were much more complicated. For the hollow Au@PtNP, the hollow structure began to shrink during its first stage melting and collapsed with the melting of Au core at around 1140 K (see the second and third snapshots of Figure 3a), thus resulting in the decrease of the statistical radius of Au atoms. The Pt shell basically kept its ordered arrangement although the diffusion of a minority of Pt atoms into the Au core reduced its radius slightly. As the melting proceeded into the second stage, higher temperature drove the faster diffusion of Au atoms into the Pt shell and the inverse diffusion of Pt atoms into Au core. Finally, as is aforementioned, the Au atoms were dominative in the outer layers to form a lower-energy structure, hence leading to the larger statistical radius of Au atoms than that of Pt ones (see Figure 5b). Nevertheless, the curves of the Pt@Au NP showed considerably different temperature dependences from those of Au@Pt one although they were almost the same beyond the overall melting of the NPs. In the first stage melting of the Pt@Au NP, the statistical radius of Pt atoms kept the linear increase because their fcc structure was well maintained (see the second and third snapshots of Figure 3b). In contrast, the statistical radius of Au atoms presented a jump due to the larger thermal expansion coefficient of the melted Au shell than that of the solid one. With the melting proceeding into the second stage, a considerable amount of Pt atoms around the core-shell interface became melted, resulting in a small peak in the radius curve (see Figure 5c). However, some of Pt atoms began to diffuse into the cavity and occupied the initial hollow space with the melting progressing (see the fourth snapshot of Figure 3b). Therefore, the statistical radius of Pt atoms exhibited a slight decrease. With the temperature further rising, the Pt and Au atoms were rapidly mixed. Consequently, the statistical radius of Au atoms gradually fell and that of Pt ones accordingly rose.
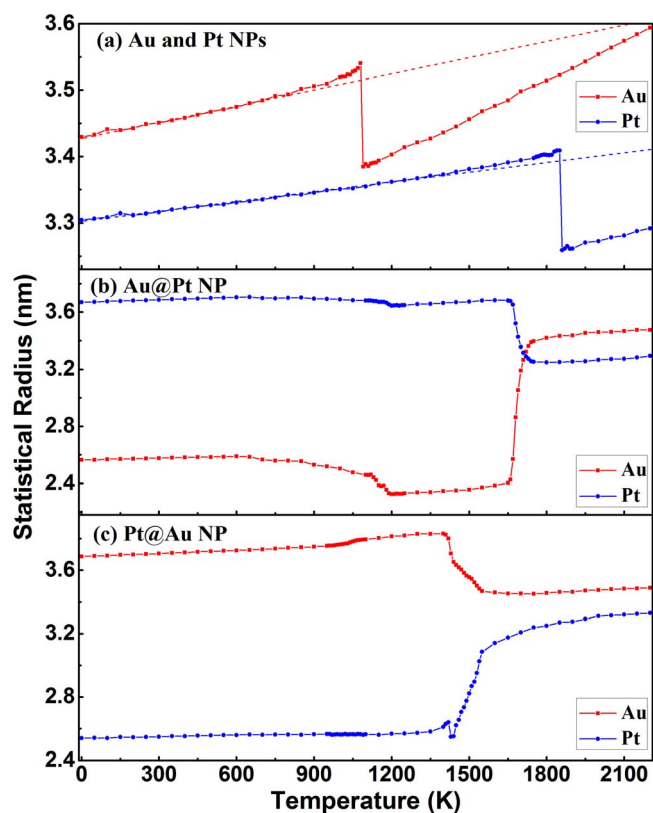
Figure 5 | Temperature dependence of statistical radius of hollow (a) monometallic Au and Pt NPs, (b) Au@Pt NP, and (c) Pt@Au NP during the continuous heating.

Conclusions

In this article, MD simulations were employed to explore the thermal stability of Au-Pt bimetallic NPs with hollow structures. The Lindemann index, common neighbor analysis, and statistical radius were adopted to examine their melting behaviors and structural evolutions during continuous heating. The major conclusions are summarized as follows.

(1) For hollow Pt@Au NP, the premelting initiates at the exterior surface and then spreads into the core. A typical two-stage melting behavior is exhibited owing to the melting point discrepancy between the core and the shell, similar to the solid ones. However, since the premelting is able to initiate at the interior surface of hollow Au@Pt NP, the two-stage melting is also presented, considerably different from the solid one. Further, the caloric curves and atomistic snapshots of the two hollow core-shell NPs indicate their diverse melting modes.

(2) The critical temperature of the first stage melting of hollow Pt@Au NP is even lower than the melting points of both hollow Au and Pt NPs. This abnormal phenomenon is originated from the existence of stacking faults at low temperatures. These stacking faults were produced after the motion of Shockley partial dislocations due to the stress step at core-shell interface, and propagated through both the core and shell.

(3) The analyses of temperature–dependent statistical radius imply that the structural collapse of hollow Au@Pt NP occurs prior to its overall melting and leads to the formation of liquid-core/solid-shell while the collapse of hollow Pt@Au NP is accompanied with its overall melting. Beyond the complete melting, both the NPs transform into mixing alloy with Au-dominated surface.

The aforementioned results provide a fundamental perspective on the thermodynamic behaviors of hollow bimetallic core-shell NPs at atomistic level. Due to the potential application of hollow structures, the current study is expected to be of significance not only to the synthesis of metallic NPs but also to the further design of novel nanostructures with both excellent performance and outstanding stability.

Methods

Model Construction. There are two types of hollow bimetallic NPs constructed from a large cubic fcc single crystal: the Au@Pt NP and the Pt@Au one. To facilitate a comparison study, hollow monometallic Au and Pt NPs were also modeled. The total number of atoms in each NP was set at 19 784, corresponding to a diameter of about 8.2 nm. Furthermore, the shell/core/hollow ratio in thickness was set to be about $1:1:2$.

MD Simulations. On the basis of our previous works[27,29,35,36], the quantum corrected Sutton-Chen (Q-SC) type potentials were adopted to describe the interatomic interactions[44]. These potentials represent many-body interactions, and their parameters were optimized according to the lattice parameter, cohesive energy, bulk modulus, elastic constants, phonon dispersion, vacancy formation energy, and surface energy, resulting in an accurate description of thermodynamic and transport properties of metals and their alloys[26,45,46]. The total potential energy for a system of atoms can be expressed as

$$U = \sum_i U_i = \sum_i \varepsilon \left[\frac{1}{2} \sum_{j \neq i} V(R_{ij}) - c\sqrt{\rho_i} \right], \quad (6)$$

in which $V(R_{ij})$ is a pair interaction function defined by the following equation

$$V(R_{ij}) = \left(\frac{a}{R_{ij}} \right)^n, \quad (7)$$

accounting for the repulsion between the i and j atomic cores; ρ_i is a local electron density accounting for cohesion associated with atom i defined by

$$\rho_i = \sum_{j \neq i} \left(\frac{a}{R_{ij}} \right)^m. \quad (8)$$

In Eqs. (6) – (8), R_{ij} is the distance between the ith and the jth atoms; a is a length parameter scaling all spacings; c is a dimensionless parameter scaling the attractive terms; ε sets the overall energy scale; n and m are integer parameters. The model parameters for Au and Pt are listed in Table 1. In order to describe the interatomic action between Au and Pt, the geometric mean was used to obtain the energy parameter ε while the arithmetic mean was used for the remaining parameters[45,46].

Upon starting molecular dynamics (MD) simulations, all NPs were first quasi-statically relaxed to a local minimum energy state through the conjugate gradients method[47]. After full relaxation, these NPs were subjected to a continuous heating process. To make the simulations more realistic, constant temperature and pressure molecular dynamics (NPT-MD) were employed to allow energy and volume fluctuations, which may be critical to the resulting dynamics. These NPs underwent a heating process composed of a series of NPT-MD simulations from 0 to 2200 K with a temperature increment of 50 K. However, a smaller step of 10 K was adopted to examine the melting behavior more accurately when the temperature was close to the melting point. At each temperature, the MD simulations were carried out for 200 *ps*, during which atomic coordinates, velocities, and energies were extracted for calculation of the statistical quantities in the last 25 *ps*. The desired temperature and ambient pressure were maintained by Nose-Hoover thermostat[48] and Berendsen approach[49], respectively. The equations of atomic motion were integrated by the Verlet-velocity algorithm[50] with a 1 *fs* time step.

1. Bell, A. T. The impact of nanoscience on heterogeneous catalysis. *Science* **299**, 1688–1691 (2003).
2. Arenz, M. *et al.* The effect of the particle size on the kinetics of CO electrooxidation on high surface area Pt catalysts. *J. Am. Chem. Soc.* **127**, 6819–6829 (2005).
3. Bianchini, C. & Shen, P. K. Palladium-based electrocatalysts for alcohol oxidation in half cells and in direct alcohol fuel cells. *Chem. Rev.* **109**, 4183–4206 (2009).
4. Xiang, Y. *et al.* Formation of rectangularly shaped Pd/Au bimetallic nanorods: evidence for competing growth of the Pd shell between the {110} and {100} side facets of Au nanorods. *Nano. Lett.* **6**, 2290–2294 (2006).

Table 1 | Potential parameters used in atomistic simulations for Au-Pt bimetallic NPs[44]

Component	n	m	$\varepsilon(meV)$	c	a (Å)
Au	11	8	7.8052	53.581	4.0651
Pt	11	7	9.7894	71.336	3.9163

5. Tao, F. *et al.* Reaction-driven restructuring of Rh-Pd and Pt-Pd core-shell nanoparticles. *Science* **322**, 932–934 (2008).

6. Ataee-Esfahani, H., Wang, L., Nemoto, Y. & Yamauchi, Y. Synthesis of bimetallic Au@Pt nanoparticles with Au core and nanostructured Pt shell toward highly active electrocatalysts. *Chem. Mater.* **22**, 6310–6318 (2010).

7. Koenigsmann, C. *et al.* Enhanced electrocatalytic performance of processed, ultrathin, supported Pd-Pt core-shell nanowire catalysts for the oxygen reduction reaction. *J. Am. Chem. Soc.* **133**, 9783–9795 (2011).

8. Wang, L. & Yamauchi, Y. Strategic synthesis of trimetallic Au@Pd@Pt core-shell nanoparticles from poly(vinylpyrrolidone)-based aqueous solution toward highly active electrocatalysts. *Chem. Mater.* **23**, 2457–2465 (2011).

9. Alayoglu, S., Nilekar, A. U., Mavrikakis, M. & Eichhorn, B. Ru-Pt core-shell nanoparticles for preferential oxidation of carbon monoxide in hydrogen. *Nat. Mater.* **7**, 333–338 (2008).

10. Liu, C. W., Wei, Y. C., Liu, C. C. & Wang, K. W. Pt-Au core/shell nanorods: preparation and applications as electrocatalysts for fuel cells. *J. Mater. Chem.* **22**, 4641–4644 (2012).

11. Li, H. J., Wu, H. X., Zhai, Y. J., Xu, X. L. & Jin, Y. D. Synthesis of monodisperse plasmonic Au core-Pt shell concave nanocubes with superior catalytic and electrocatalytic activity. *ACS Cata.* **3**, 2045–2051 (2013).

12. Lu, C. L., Prasad, K. S., Wu, H. L., Ho, J. A. & Huang, M. H. Au Nanocube-directed fabrication of Au-Pd core-shell nanocrystals with tetrahexahedral, concave octahedral, and octahedral structures and their electrocatalytic activity. *J. Am. Chem. Soc.* **132**, 14546–14553 (2010).

13. Mahmoud, M. A., Saira, F. & El-Sayed, M. A. Experimental evidence for the nanocage effect in catalysis with hollow nanoparticles. *Nano Lett.* **10**, 3764–3769 (2010).

14. Peng, Z. M., You, H. J., Wu, J. B. & Yang, H. Electrochemical synthesis and catalytic property of sub-10 nm platinum cubic nanoboxes. *Nano Lett.* **10**, 1492–1496 (2010).

15. Chen, G., Desinan, S., Rosei, R., Rosei, F. & Ma, D. Hollow ruthenium nanoparticles with small dimensions derived from Ni@Ru core@shell structure: synthesis and enhanced catalytic dehydrogenation of ammonia borane. *Chem. Commun.* **48**, 8009–8011 (2012).

16. Selvakannan, P. R. & Sastry, M. Hollow gold and platinum nanoparticles by a transmetallation reaction in an organic solution. *Chem. Commun.* **13**, 1684–1686 (2005).

17. Dowgiallo, A. M. & Knappenberger, Jr, K. L. Ultrafast electron−phonon coupling in hollow gold nanospheres. *Phys. Chem. Chem. Phys.* **13**, 21585–21592 (2011).

18. Dowgiallo, A. M., Schwartzberg, A. M. & Knappenberger, Jr, K. L. Structure−dependent coherent acoustic vibrations of hollow gold nanospheres. *Nano Lett.* **11**, 3258–3262 (2011).

19. Song, H. M., Anjum, D. H., Sougrat, R., Hedhili, M. N. & Khashab, N. M. Hollow Au@Pd and Au@Pt core-shell nanoparticles as electrocatalysts for ethanol oxidation reactions. *J. Mater. Chem.* **22**, 25003–25010 (2012).

20. Wang, L. & Yamauchi, Y. Metallic Nanocages: Synthesis of bimetallic Pt–Pd hollow nanoparticles with dendritic shells by selective chemical etching. *J. Am. Chem. Soc.* **135**, 16762–16765 (2013).

21. Sun, Q., Ren, Z., Wang, R. M., Wang, N. & Cao, X. Platinum catalyzed growth of NiPt hollow spheres with an ultrathin shell. *J. Mater. Chem.* **21**, 1925–1930 (2011).

22. Zhang, X., Zhang, G. Y., Zhang, B. D. & Su, Z. H. Synthesis of hollow Ag-Au bimetallic nanoparticles in polyelectrolyte multilayers. *Langmuir* **29**, 6722–6727 (2013).

23. Wang, M. *et al.* PdNi hollow nanoparticles for improved electrocatalytic oxygen reduction in alkaline environments. *ACS Appl. Mater. Inter.* **5**, 12708–12715 (2013).

24. Liu, H. & Yang, J. Bimetallic Ag-hollow Pt heterodimers via inside-out migration of Ag in core-shell Ag-Pt nanoparticles at elevated temperature. *J. Mater. Chem. A* **2**, 7075–7081 (2014).

25. Li, S. S. *et al.* Simple synthesis of hollow Pt-Pd nanospheres supported on reduced graphene oxide for enhanced methanol electrooxidation. *J. Power Sources* **254**, 119–125 (2014).

26. Qi, Y., Cagin, T., Johnson, W. L. & Goddard, W. A. Melting and crystallization in Ni nanoclusters: the mesoscale regime. *J. Chem. Phys.* **115**, 385–394 (2001).

27. Huang, R., Wen, Y. H., Zhu, Z. Z. & Sun, S. G. Two-stage melting in core-shell nanoparticles: an atomic-scale perspective. *J. Phys. Chem. C* **116**, 11837–11841 (2012).

28. Kittel, C. *Introduction to Solid State Physics* (John Wiley & Sons, New York, 1996).

29. Huang, R., Wen, Y. H., Shao, G. F. & Sun, S. G. Insight into the melting behavior of Au−Pt core−shell nanoparticles from atomistic simulations. *J. Phys. Chem. C* **117**, 4278–4286 (2013).

30. Shibuta, Y. & Suzuki, T. Melting and nucleation of iron nanoparticles: a molecular dynamics study. *Chem. Phys. Lett.* **445**, 265–270 (2007).

31. Löwen, H. Melting, freezing and colloidal suspensions. *Phys. Rep.* **237**, 249–260 (1994).

32. Zhou, Y. Q., Karplus, M., Ball, K. D. & Berry, R. S. The distance fluctuation criterion for melting: comparison of square-well and Morse potential models for clusters and homopolymers. *J. Chem. Phys.* **116**, 2323–2329 (2002).

33. Sun, Y. G. & Xia, Y. N. Shape-controlled synthesis of gold and silver nanoparticles. *Science* **298**, 2176–2179 (2002).

34. Tyson, W. R. & Miller, W. A. Surface free energies of solid metals: estimation from liquid surface tension measurements. *Surf. Sci.* **62**, 267–276 (1977).

35. Huang, R., Wen, Y. H., Zhu, Z. Z. & Sun, S. G. Pt-Pd bimetallic catalysts: structural and thermal stabilities of core-shell and alloyed nanoparticles. *J. Phys. Chem. C* **116**, 8664–8671 (2012).

36. Huang, R., Wen, Y. H., Shao, G. F., Zhu, Z. Z. & Sun, S. G. Thermal stability and shape evolution of tetrahexahedral Au-Pd core-shell nanoparticles with high-index facets. *J. Phys. Chem. C* **117**, 6896–6903 (2013).

37. Honeycutt, J. D. & Andersen, H. C. Molecular dynamics study of melting and freezing of small Lennard-Jones clusters. *J. Phys. Chem.* **91**, 4950–4963 (1987).

38. Schiøtz, J., Di Tolla, F. D. & Jacobsen, K. W. Softening of Nanocrystalline Metals at very small grain sizes. *Nature* **391**, 561–563 (1998).

39. Wen, Y. H., Zhang, Y., Zheng, J. C., Zhu, Z. Z. & Sun, S. G. Orientation-dependent structural transition and melting of Au nanowires. *J. Phys. Chem. C* **113**, 20611–20617 (2009).

40. Schiøtz, J., Vegge, T., Di Tolla, F. D. & Jacobsen, K. W. Atomic-scale simulations of the mechanical deformation of nanocrystalline metals. *Phys. Rev. B* **60**, 11971–11983 (1999).

41. Mottet, C., Rossi, G., Baletto, F. & Ferrando, R. Single impurity effect on the melting of nanoclusters. *Phys. Rev. Lett.* **95**, 035501 (2005).

42. Brandes, E. A. & Brook, G. B. *Smithells Metal Reference Book* (Butterworth-Heinemann, Boston, 1992).

43. Li, W. H. *et al.* Thermal contraction of Au nanoparticles. *Phys. Rev. Lett.* **89**, 135504 (2002).

44. Cagin, T. *et al.* Calculation of mechanical, thermodynamic and transport properties of metallic glass formers. *Mater. Res. Soc. Symp. Proc.* **554**, 43–48 (1998).

45. Ikeda, H. *et al.* Strain rate induced amorphization in metallic nanowires. *Phys. Rev. Lett.* **82**, 2900–2903 (1999).

46. Sankaranarayanan, S. K. R. S., Bhethanabotla, V. R. & Joseph, B. Molecular dynamics simulation study of the melting of Pd-Pt nanoclusters. *Phys. Rev. B* **71**, 195415 (2005).

47. Leach, A. R. *Molecular Modelling: Principles and Applications* (Pearson Education-Hall, London, 2001).

48. Evans, D. L. & Holian, B. L. The Nose-Hoover thermostat. *J. Chem. Phys.* **83**, 4069–4074 (1985).

49. Berendsen, H. J. C., Postma, J. P. M., van Gunsteren, W. F., DiNola, A. & Haak, J. R. Molecular dynamics with coupling to an external bath. *J. Chem. Phys.* **81**, 3684–3690 (1984).

50. Swope, W. C., Anderson, H. C., Berens, P. H. & Wilson, K. R. A computer simulation method for the calculation of equilibrium constants for the formation of physical clusters of molecules: application to small water clusters. *J. Chem. Phys.* **76**, 637–649 (1982).

Acknowledgments

Author contributions

R.H. performed most of the simulations. G.F.S and X.M.Z. prepared the figures. Y.H.W. was responsible for the manuscript. All authors contributed to analysis of the results.

Additional information

Competing financial interests: The authors declare no competing financial interests.

How to cite this article: Huang, R., Shao, G.-F., Zeng, X.-M. & Wen, Y.-H. Diverse Melting Modes and Structural Collapse of Hollow Bimetallic Core-Shell Nanoparticles: A Perspective from Molecular Dynamics Simulations. *Sci. Rep.* **4**, 7051; DOI:10.1038/srep07051 (2014).